Organic Electronics 110 (2022) 106642

Contents lists available at ScienceDirect

Organic Electronics

journal homepage: www.elsevier.com/locate/orgel

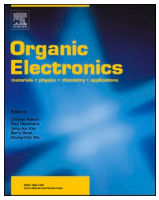

A near-infrared acceptor incorporating selenium heterocycles for efficient semi-transparent photovoltaics and sensitive photodetectors

Yuzhong Huang, Changzun Jiang, Yu Zhu, Shuchao Zhang, Guanghui Li, Zhaoyang Yao, Chenxi Li, Xiangjian Wan *, Yongsheng Chen **

The Centre of Nanoscale Science and Technology and Key Laboratory of Functional Polymer Materials, Institute of Polymer Chemistry, State Key Laboratory of Elemento-Organic Chemistry, Haihe Laboratory of Sustainable Chemical Transformations College of Chemistry, Renewable Energy Conversion and Storage Center (RECAST), Nankai University, Tianjin, 300071, China

ARTICLE INFO

Keywords:
Organic solar cells
Near-infrared acceptor
Semi-transparent photovoltaics
Organic photodetector
Selenium heterocycles

ABSTRACT

Near infrared (NIR) acceptors are the key components for the construction of efficient organic photovoltaics (OPVs) and organic photodetectors (OPDs). Herein, a near-infrared acceptor named 6TSe-OFIC incorporating selenium heterocycles has been designed, which shows an absorption onset around 1000 nm with a low optical bandgap of 1.29 eV. OPV device based on PCE10: 6TSe-OFIC demonstrates a power conversion efficiency (PCE) of 13.18% with a high and broad EQE response. The semi-transparent OPV device based on PCE10: 6TSe-OFIC shows a PCE of 10.06% with AVT 20%. With the same active layer, the OPD devices achieve the responsivities of 0.54 A W^{-1} at ~850 nm. The results highlight the opportunities to careful design of the NIR molecules for efficient OPVs and OPDs.

1. Introduction

Organic semiconductor materials with the near-infrared (NIR) absorptions are of critical importance in organic electronic devices such as organic photovoltaics (OPVs), organic photodetectors (OPDs) and etc. The state-of-the-art OPVs have achieved the impressive efficiencies over 18% mainly thanks to the invention of new active layer materials especially non fullerene acceptors (NFAs) with broad absorptions up to near-infrared range [1–9]. Meanwhile, with the similar device structure and working principles, NIR OPDs have demonstrated great potentials in health monitoring, artificial vision, optical communication networks and etc [10–12]. Clearly, NIR acceptors are the key component materials for constructing efficient OPVs and OPDs with the bulk heterojunction structure. In the past decade, enormous attentions have been drawn on the design of NFAs, especially those with the acceptor-donor-acceptor (A-D-A) architectures [13–17]. The physical properties of A-D-A type molecules such as absorption, energy levels and etc. Can be finely tuned via the chemical structure modulation of the central core, side chains or end groups. Indeed, the strategy of A-D-A architecture has given great opportunities and made much success for the molecule design and corresponding molecular property tuning [18–23]. However, most of reported efficient NIR acceptors including the wide studied Y6 derivatives show the absorption edge around 930 nm [1,6,24–28]. It is still high desirable to develop efficient NIR acceptors with absorption region extended to longer wavelength. Among the strategies for design NIR molecules, incorporating selenium in the molecule backbone has proved to be an effective way. Compared with sulfur atom, selenium atom has the larger atom radius, more polarized and delocalized electron clouds [29–38]. Thus, the strong intermolecular interactions are expected, which facilitates the molecular packing and reduces the molecular band gap.

In this work, we report a NIR acceptor named 6TSe-OFIC (Fig. 1a), which is designed based on the acceptor 6T-OFIC we previously reported. After introducing Se in the backbone, 6TSe-OFIC shows clearly redshifted film absorption with onset around 1000 nm compared with that of 6T-OFIC. The photovoltaic devices based on PCE10: 6TSe-OFIC shows a PCE of 13.18%, which among the best results of NIR acceptors with absorption edge of 1000 nm. Besides, the semitransparent OPV devices based on PCE10: 6TSe-OFIC delivered a PCE of 10.06% with average visible transmittance (AVT) of 20.5%. Moreover, the OPDs based on the PCE10: 6TSe-OFIC gave a high responsivity of 0.55 A W^{-1} (850 nm) under zero bias, with a low dark current density (J_d) of 0.64

* Corresponding author.
** Corresponding author.
E-mail addresses: xjwan@nankai.edu.cn (X. Wan), yschen99@nankai.edu.cn (Y. Chen).

https://doi.org/10.1016/j.orgel.2022.106642
Received 14 July 2022; Received in revised form 2 September 2022; Accepted 6 September 2022
Available online 11 September 2022

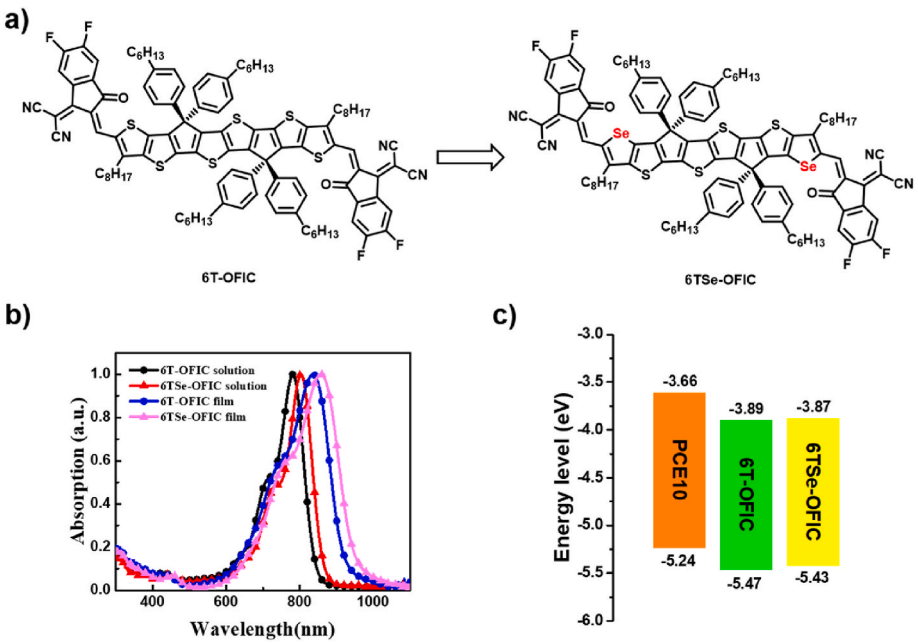

Fig. 1. (a) Chemical structures of 6T-OFIC and 6TSe-OFIC. (b) UV–vis absorption spectra of 6T-OFIC and 6TSe-OFIC. (c) Energy levels of PCE10, 6T-OFIC and 6TSe-OFIC.

Table 1
The optical and electrochemical properties of 6TSe-OFIC and 6T-OFIC.

Comp.	λ_{max}^{sol} (nm)	λ_{max}^{film} (nm)	HOMO (eV)	LUMO (eV)	λ_{onset}^{film} (nm)	E_g^{opt} (eV)
6T-OFIC	780	835	−5.47	−3.89	946	1.31
6TSe-OFIC	802	856	−5.43	−3.87	960	1.29

nA cm^{-2} and a good shot-noise limited specific detectivity Dsh* of over 10^{12} from 400 to 960 nm with a peak of 3.77 × 10^{12} jones at 850 nm, which is among the high efficiency self-powered OPDs and close to that of commercial silicon detectors.

2. Result and discussion

2.1. Property of material and device performance

The synthesis of 6TSe-OFIC is conducted with the similar procedure of 6T-OFIC we have previously reported [39]. The detailed synthesis procedures and characterization are provided in the supporting information. The UV–vis absorption spectra of 6TSe-OFIC and 6T-OFIC are shown in Fig. 1b. Clearly, with incorporating Se, 6TSe-OFIC demonstrates redshifted absorptions in solution and solid film compared with 6T-OFIC. In chloroform solution, 6TSe-OFIC shows the maximum absorption (λ_{max}) peak located at 802 nm. In solid film, it redshifts by 54 nm with λ_{max} at 856 nm. In contrast, 6T-OFIC shows λ_{max} of 780 nm in CF solution and 835 in solid film. The optical bandgaps (E_g^{opt}) of 6T-OFIC and 6TSe-OFIC calculated from their thin-film absorption edge are 1.31 and 1.29 eV, corresponding to λ_{onset} of 946 and 960 nm, respectively. The energy levels of the two molecules were investigated by

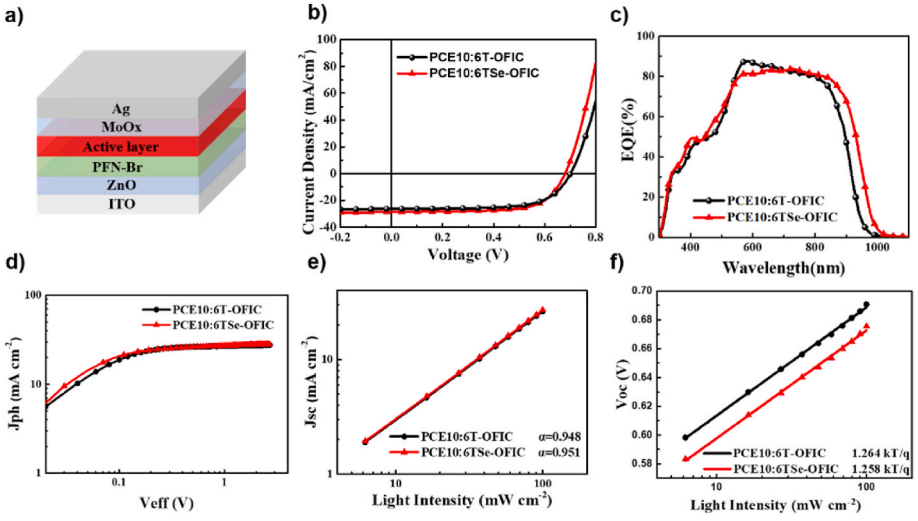

Fig. 2. (a) Device architecture of the two blends. (b) J-V and c) EQE curve for the optimized device. (d) Jph versus Veff characteristics. (e) Jsc and f) Voc versus light intensity of the optimized devices.

Table 2
The optimal photovoltaic parameters of PCE10:6T-OFIC and PCE10:6TSe-–OFIC–based devices under AM 1.5G Illumination (100 mW cm^{-2}).

Active layer	V_{oc} (V)	J_{sc} (mA/cm^2)	FF (%)	PCE (%)[a]
PCE10:6T-OFIC	0.701 (0.696 ± 0.004)	26.35 (26.53 ± 0.38)	66.90 (66.32 ± 0.72)	12.37 (12.25 ± 0.27)
PCE10:6TSe-OFIC	0.676 (0.673 ± 0.004)	27.67 (27.68 ± 0.35)	70.27 (69.84 ± 0.67)	13.18 (13.04 ± 0.19)

[a] Statistical and optimal results are listed outside of parentheses and in parentheses, respectively, and the average parameters were calculated from 10 independent cells.

Table 3
Summary of photovoltaic parameters of PCE10:6TSe-OFIC based ST-OPVs under AM 1.5 G irradiation (100 mW cm^{-2}).

Ag thickness (nm)	V_{oc} (V)	J_{sc} (mA/cm^2)	FF (%)	PCE (%)	AVT (%)	LUE
10	0.662	19.94	58.67	7.82	21.6	1.69
15	0.673	21.70	68.27	10.06	20.5	2.06
20	0.675	24.85	70.50	11.93	12.7	1.52

electrochemical cyclic voltammetry (CV). From the onset reduction and oxidation potentials of the CV curves, the highest occupied molecular orbital (HOMO) level and the lowest unoccupied molecular orbit (LUMO) energy levels were estimated to be −5.43 and −3.87 eV for 6TSe-OFIC, −5.47 and −3.89 eV for 6T-OFIC (Fig. 1c, Table 1). Compared with 6 T-OFIC, 6TSe-OFIC has the lower HOMO level and thus slightly reduced bandgap.

The OPV devices with the inverted structure of indium tin oxide (ITO)/ZnO/PFN-Br/active layers/MoOx/Ag (Fig. 2a) were fabricated to evaluate the photovoltaic performance of the NIR acceptor 6TSe-OFIC together with 6TSe-OFIC for comparison. The low bandgap polymer PCE10 was selected as donor owing to its matched energy levels with the two NIR acceptors. The details of device fabrication are presented in the supporting information. The current density-voltage (J-V) curves of the optimized devices are illustrated in Fig. 2b and the corresponding photovoltaic parameters are listed in Table 2. The optimal device of PCE10:6T-OFIC showed a PCE of 12.37% with a Voc of 0.701 V, a Jsc of 26.35 mA cm^{-2} and a FF of 66.90%. In contrast, the device of PCE10:6TSe-OFIC achieved a PCE of 13.18%, which was mainly attributed to the enhanced Jsc of 27.67 mA cm^{-2} and FF of 70.27%. The external quantum efficiency (EQE) curve of the two devices are illustrated in Fig. 2c. The two devices all featured the high photon response with wide range, especially for that of 6TSe-OFIC with EQE responding range from 300 to around 1000 nm. The integrated Jsc from the EQE curves are 25.22 and 26.47 mA cm^{-2} for the 6T-OFIC and 6TSe-–OFIC–based devices, respectively, which agree well with the Jsc measured in the J-V curves. In addition, the initial stability of the two devices were measured in the glove box in Ar without encapsulation. As shown in Fig. S4, the two devices retained 90% of their initial efficiencies after 200 h with thermal treatment under 65 °C or without thermal treatment, demonstrating the good thermal and storage stabilities.

The properties of the charge transport, exciton dissociation and charge generation of the two devices were investigated. The charge mobilities of the two blend films were studied using the space-charge-limited current (SCLC) method [40]. As summarized in Table S1, the electron/hole mobilities were calculated to be $4.40 \times 10^{-4}/0.77 \times 10^{-4}$ and $3.06 \times 10^{-4}/1.91 \times 10^{-4}$ cm^{-2} V^{-1} s^{-1} for the blend of PCE10:6T-OFIC and PCE10:6TSe-OFIC, respectively. The blend of PCE10:6TSe-OFIC showed higher electron mobility and more balanced electron/hole ratio of 1.60, which are beneficial to promote charge transport and contribute to the higher FF and J_{sc} of the PCE10:6TSe-OFIC based devices. Furtherly, in order to investigate the exciton dissociation and charge generation properties, the dependence of photocurrent density (J_{ph}) versus effective voltage (V_{eff}) were measured for the two devices (Fig. 2d). The exciton dissociation probability (P_{diss}), calculated from J_{ph} under the short-circuit condition divided by the saturated photocurrent density (J_{sat}) [41], were 96.71 and 94.65% for 6TSe-OFIC and 6T-OFIC based devices, respectively, demonstrating higher efficient exciton dissociation for the 6TSe-OFIC based device. To study the behaviour of charge recombination of the two devices, the plots of light-intensity dependence (P) of J_{sc} ($J_{sc} \propto P^{\alpha}$, where the exponent of α being close to 1 reflects a weak bimolecular recombination [42–46]) were measured to be 0.951 and 0.948 for 6TSe-OFIC and 6T-OFIC based devices (Fig. 2e), respectively, indicating that bimolecular recombination is effectively suppressed, especially for 6TSe-OFIC based devices. Fig. 3f shows the relationship between the light intensity and V_{oc}. The slope was calculated to be $1.264kT/q$ and $1.258kT/q$ for PCE10:6T-OFIC and PCE10:6TSe-OFIC, respectively, indicating that two devices both have less trap-assisted recombination losses. In addition, the carrier lifetime of the two devices were measured using the transient photovoltage (TPV) technique. As shown in Fig. S5, the PCE10:6TSe-OFIC device has longer carrier lifetime (46μs) than that of the PCE10:6T-OFIC device (37μs), indicating the efficient suppression of bimolecular recombination for the 6TSe-OFIC based device.

Atomic force microscopy (AFM) and grazing incidence wide-angle X-ray scattering (GIWAXS) were used to investigated the morphologies of the two acceptors blend film. As illustrated in Fig. S1, the two blend films all showed smooth surfaces morphologies with fibrillar networks. The root-mean-square roughness (R_q) values are 0.85 nm and 1.12 nm for 6TSe-OFIC and 6T-OFIC based blend films, respectively. From the GIWAXS (Fig. S2), the 6T-OFIC and 6TSe-OFIC blend films all show the clear lamellar stacking peak in the out of plane (OOP) direction, indicating the face-on dominant orientation. Compared with 6T-OFIC, 6TSe-OFIC neat film shows the intense π-π stacking with distance of 3.70 Å, demonstrating that incorporating Se favors the intermolecular packing. In the blend films, the CCL of the PCE10:6TSe-OFIC film is 28.4 Å similar to that of the PCE10:6T-OFIC film (28.5 Å).

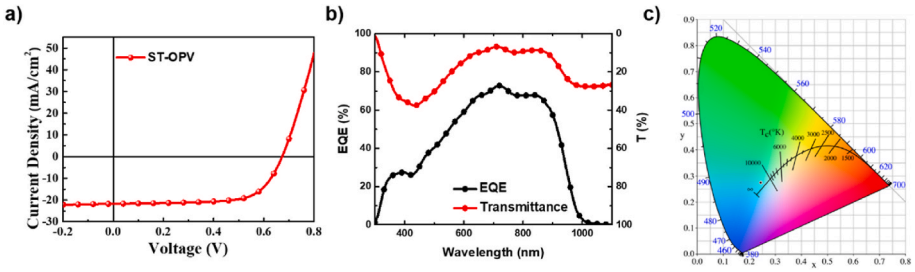

Fig. 3. (a) J–V curve of PCE10:6TSe-OFIC based ST-OPV with 15 nm Ag. (b) EQE, transmittance spectrum and (c) Representation of the color coordinates (x, y) of the ST-OPV under standard D65 illumination light source on the CIE 1931 color space.

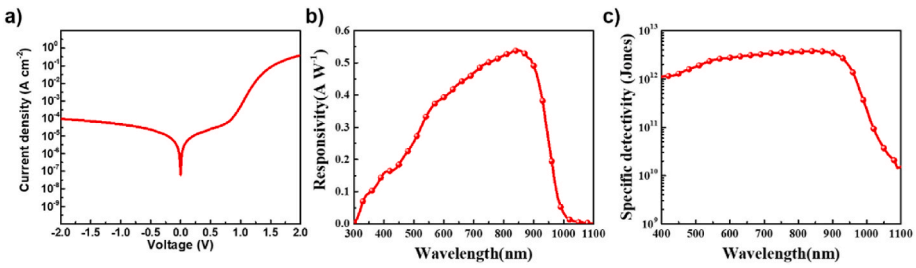

Fig. 4. (a) J–V curve of the device in the dark. (b) Responsivity, (c) shot-noise-limited specific detectivity of the device at 0 V.

2.2. Semi-transparency OPV

The high efficiency and broad NIR response of the device based on 6TSe-OFIC enable it to be used in semi-transparent OPVs (ST-OPVs). We fabricated a series of ST-OPVs with different thicknesses of the Ag electrode with the optimized PCE10: 6TSe-OFIC as the active layer. The current density-voltage (J-V) curves of the optimized device are illustrated in Fig. 3a and the detailed photovoltaic parameters of the ST-OPVs are listed in Table 3. The devices with Ag electrode thickness of 20 nm, 15 nm and 10 nm showed the PCEs of 11.93%, 10.06% and 7.82%, respectively. The gradually decreased PCEs are attributed to the reduced light reflection and decreased electrical conductivity of the Ag layer with reducing the thickness of the Ag electrode. The average visible transmittance (AVT) was calculated by the equation: AVT=($\int$T(λ)P(λ)S(λ)dλ)/($\int$P(λ)S(λ)dλ), where λ is the wavelength, T(λ) is the transmission of the device (Fig. 3b), P(λ) is the photopic response for human eyes, and S(λ) is the solar photon flux (AM 1.5G), resulting in AVTs of 12.7%, 20.5% and 21.6% for the three devices with Ag electrode thickness of 20 nm, 15 nm and 10 nm, respectively. The light utilization efficiency (LUE), calculated by LUE = PCE × AVT, are 1.52, 2.06 and 1.27 for the devices with 20 nm, 15 nm, and 10 nm Ag electrodes, respectively. The LUE 2.06 for the 15 nm Ag based device is among the excellent values of the ST-OPVs without optical modulation. Moreover, the color coordinates (x, y), correlative color temperature (CCT) and color rendering index (CRI) on the CIE 1931 chromaticity diagram (Fig. 3c) were calculated to evaluate the transparency perception of the 15 nm Ag based device. The ST-OPV with 15 nm Ag electrode showed a CIE color coordinates of (0.244, 0.275), a CCT of 16265K and a good color rendering property with CRI of 90.4.

2.3. Photodetector performance

Considering the high and broad EQE response of 6TSe-OFIC based OPV, we examined its function in NIR OPDs. Fig. 4a shows the current–voltage (J–V) curve in the dark of the device. The OPDs were fabricated using the same structure of the solar cell devices. Responsivity (R), the ratio of the photocurrent to the incident light intensity, is an important parameter to evaluate the response of a photodetector. R is calculated from the EQE according to the equation: R = EQE × λ/1240, where λ is the wavelength of the incident light in nanometer [47]. Fig. 4b depicts the spectral responsivity of the PCE10: 6TSe-OFIC based devices measured under zero bias. The responsivity of the OPD peaks at 0.54 A W^{-1} at 850 nm, which is among the highest responsivity in the NIR OPDs without additional gain mechanisms [48–56]. In addition, the dark current density as low as 0.64 nA cm^{-2} is calculated from the J-V semi-log plot of the device under dark conditions (Fig. 4a), indicating the excellent sensitivity of the NIR OPD.

The specific detectivity (D*) depicts the sensitivity of a photodetector to weak optical signals. It is given by the following equation.

$$D^* = \frac{R\sqrt{AB}}{i_n} = \frac{R\sqrt{A}}{S_n}$$

where A is the active device area in cm^2, B is the bandwidth in Hz, i_n is the noise current in A, and S_n is the noise current spectral density in A Hz$^{-1/2}$. The S_n can be calculated from the current–voltage characteristics in the dark condition with the assumption that the shot noise is the main contributor to the total noise. Accordingly, the shot-noise-limited specific detectivity (D_{sh}*) can be obtained by the following equation.

$$D^*_{sh} = \frac{R\sqrt{AB}}{i_{sh}} = \frac{R}{\sqrt{2qJ_d}}$$

where i_{sh} is the shot noise current and q is the elementary charge. According to equation above, D_{sh}* of 6TSe-OFIC based OPD was calculated (Fig. 4c). The OPD device demonstrates a D_{sh}* value of over 10^{12} jones from 400 to 960 nm with a peak of 3.77 × 10^{12} jones at 850 nm. The photo-response time was measured to be 450 ns under 850 nm infrared light modulated at 100 kHz (Fig. S6).

3. Conclusion

In summary, we have designed and synthesized a NIR acceptor 6TSe-OFIC incorporating Se in the molecular backbone, which is one of the few acceptors with high photo response in the NIR region with the absorption onset around 1000 nm. The OPV device based on PCE10:6TSe-OFIC shows a PCE over 13% and a J_{sc} of 27.67 mA cm^{-2} with a high and broad NIR EQE response. The semi-transparent device of PCE10:6TSe-OFIC achieves a PCE of 10.06% with an AVT over 20%. Moreover, the self-powered OPD device of PCE10:6TSe-OFIC demonstrates the responsivities of 0.54 A W^{-1} at ~850 nm, with a low dark current density of 0.64 nA cm^{-2} and a shot-noise-limited specific detectivity of over 10^{12} jones from 400 to 960 nm. The results indicate that the careful structural modification via Se substitution can fine tune the properties of NFAs and offer more opportunities for NFA design for application in OPVs and OPDs.

Declaration of competing interest

The authors declare that they have no known competing financial interests or personal relationships that could have appeared to influence the work reported in this paper.

Data availability

Data will be made available on request.

Acknowledgements

The authors gratefully acknowledge the financial support from NSFC (52025033 and 21935007), MoST (2019YFA0705900) of China, Tianjin city (20JCZDJC00740), 111 Project (B12015) and Haihe Laboratory of Sustainable Chemical Transformations.

Appendix A. Supplementary data

Supplementary data to this article can be found online at https://doi.org/10.1016/j.orgel.2022.106642.

References

[1] Y. Cui, Y. Xu, H. Yao, P. Bi, L. Hong, J. Zhang, Y. Zu, T. Zhang, J. Qin, J. Ren, Z. Chen, C. He, X. Hao, Z. Wei, J. Hou, Single-junction organic photovoltaic cell with 19% efficiency, Adv. Mater. 33 (2021), 2102420.

[2] C. Guo, D. Li, L. Wang, B. Du, Z.-X. Liu, Z. Shen, P. Wang, X. Zhang, J. Cai, S. Cheng, C. Yu, H. Wang, D. Liu, C.-Z. Li, T. Wang, Cold-aging and solvent vapor mediated aggregation control toward 18% efficiency binary organic solar cells, Adv. Energy Mater. 11 (2021), 2102000.

[3] L. Hong, H. Yao, Y. Cui, P. Bi, T. Zhang, Y. Cheng, Y. Zu, J. Qin, R. Yu, Z. Ge, J. Hou, 18.5% efficiency organic solar cells with a hybrid planar/bulk heterojunction, Adv. Mater. 33 (2021), 2103091.

[4] C. Li, J. Zhou, J. Song, J. Xu, H. Zhang, X. Zhang, J. Guo, L. Zhu, D. Wei, G. Han, J. Min, Y. Zhang, Z. Xie, Y. Yi, H. Yan, F. Gao, F. Liu, Y. Sun, Non-fullerene acceptors with branched side chains and improved molecular packing to exceed 18% efficiency in organic solar cells, Nat, Energy 6 (2021) 605–613.

[5] Y. Lin, M.I. Nugraha, Y. Firdaus, A.D. Scaccabarozzi, F. Aniés, A.-H. Emwas, E. Yengel, X. Zheng, J. Liu, W. Wahyudi, E. Yarali, H. Faber, O.M. Bakr, L. Tsetseris, M. Heeney, T.D. Anthopoulos, A simple n-dopant derived from diquat boosts the efficiency of organic solar cells to 18.3, ACS Energy Lett. 5 (2020) 3663–3671.

[6] F. Liu, L. Zhou, W. Liu, Z. Zhou, Q. Yue, W. Zheng, R. Sun, W. Liu, S. Xu, H. Fan, L. Feng, Y. Yi, W. Zhang, X. Zhu, Organic solar cells with 18% efficiency enabled by an alloy acceptor: a two-in-one strategy, Adv. Mater. 33 (2021), 2100830.

[7] L. Liu, S. Chen, Y. Qu, X. Gao, L. Han, Z. Lin, L. Yang, W. Wang, N. Zheng, Y. Liang, Y. Tan, H. Xia, F. He, Nanographene–osmapentalyne complexes as a cathode interlayer in organic solar cells enhance efficiency over 18, Adv. Mater. 33 (2021), 2101279.

[8] H. Meng, C. Liao, M. Deng, X. Xu, L. Yu, Q. Peng, 18.77 % efficiency organic solar cells promoted by aqueous solution processed cobalt(II) acetate hole transporting layer, Angew. Chem. Int. Ed. 60 (2021) 22554–22561.

[9] J. Zhang, F. Bai, I. Angunawela, X. Xu, S. Luo, C. Li, G. Chai, H. Yu, Y. Chen, H. Hu, Z. Ma, H. Ade, H. Yan, Alkyl-chain branching of non-fullerene acceptors flanking conjugated side groups toward highly efficient organic solar cells, Adv. Energy Mater. 11 (2021), 2102596.

[10] F.P. García de Arquer, A. Armin, P. Meredith, E.H. Sargent, Correction: corrigendum: Solution-processed semiconductors for next-generation photodetectors, Nat. Rev. Mater. 2 (2017), 17012.

[11] X. Liu, Y. Lin, Y. Liao, J. Wu, Y. Zheng, Recent advances in organic near-infrared photodiodes, J. Mater. Chem. C 6 (2018) 3499–3513.

[12] Z. Wu, Y. Zhai, H. Kim, J.D. Azoulay, T.N. Ng, Emerging design and characterization guidelines for polymer-based infrared photodetectors, Acc. Chem. Res. 51 (2018) 3144–3153.

[13] Y. Chen, X. Wan, G. Long, High performance photovoltaic applications using solution-processed small molecules, Acc. Chem. Res. 46 (2013) 2645–2655.

[14] P. Cheng, G. Li, X. Zhan, Y. Yang, Next-generation organic photovoltaics based on non-fullerene acceptors, Nat. Photonics 12 (2018) 131–142.

[15] Y. Xu, H. Yao, J. Hou, Recent advances in fullerene-free polymer solar cells: materials and devices, Chin. J. Chem. 37 (2019) 207–215.

[16] J. Zhang, H.S. Tan, X. Guo, A. Facchetti, H. Yan, Material insights and challenges for non-fullerene organic solar cells based on small molecular acceptors, Nat. Energy 3 (2018) 720–731.

[17] W. Zhao, S. Li, H. Yao, S. Zhang, Y. Zhang, B. Yang, J. Hou, Molecular optimization enables over 13% efficiency in organic solar cells, J. Am. Chem. Soc. 139 (2017) 7148–7151.

[18] Z. Fei, F.D. Eisner, X. Jiao, M. Azzouzi, J.A. Röhr, Y. Han, M. Shahid, A.S. R. Chesman, C.D. Easton, C.R. McNeill, T.D. Anthopoulos, J. Nelson, M. Heeney, An alkylated indacenodithieno[3,2-b]thiophene-based nonfullerene acceptor with high crystallinity exhibiting single junction solar cell efficiencies greater than 13% with low voltage losses, Adv. Mater. 30 (2018), 1705209.

[19] D. He, F. Zhao, J. Xin, J.J. Rech, Z. Wei, W. Ma, W. You, B. Li, L. Jiang, Y. Li, C. Wang, A fused ring electron acceptor with decacyclic core enables over 13.5% efficiency for organic solar cells, Adv. Energy Mater. 8 (2018), 1802050.

[20] C. Huang, X. Liao, K. Gao, L. Zuo, F. Lin, X. Shi, C.-Z. Li, H. Liu, X. Li, F. Liu, Y. Chen, H. Chen, A.K.Y. Jen, Highly efficient organic solar cells based on S,N-heteroacene non-fullerene acceptors, Chem. Mater. 30 (2018) 5429–5434.

[21] X. Ke, L. Meng, X. Wan, M. Li, Y. Sun, Z. Guo, S. Wu, H. Zhang, C. Li, Y. Chen, The rational and effective design of nonfullerene acceptors guided by a semi-empirical model for an organic solar cell with an efficiency over 15, J. Mater. Chem. 8 (2020) 9726–9732.

[22] W. Liu, J. Zhang, Z. Zhou, D. Zhang, Y. Zhang, S. Xu, X. Zhu, Design of a new fused-ring electron acceptor with excellent compatibility to wide-bandgap polymer donors for high-performance organic photovoltaics, Adv. Mater. 30 (2018), 1800403.

[23] J. Sun, X. Ma, Z. Zhang, J. Yu, J. Zhou, X. Yin, L. Yang, R. Geng, R. Zhu, F. Zhang, W. Tang, Dithieno[3,2-b:2′,3′-d]pyrrol fused nonfullerene acceptors enabling over 13% efficiency for organic solar cells, Adv. Mater. 30 (2018), 1707150.

[24] L. Hong, H. Yao, Z. Wu, Y. Cui, T. Zhang, Y. Xu, R. Yu, Q. Liao, B. Gao, K. Xian, H. Y. Woo, Z. Ge, J. Hou, Eco-compatible solvent-processed organic photovoltaic cells with over 16% efficiency, Adv. Mater. 31 (2019), 1903441.

[25] K. Jiang, Q. Wei, J.Y.L. Lai, Z. Peng, H.K. Kim, J. Yuan, L. Ye, H. Ade, Y. Zou, H. Yan, Alkyl chain tuning of small molecule acceptors for efficient organic solar cells, Joule 3 (2019) 3020–3033.

[26] J. Qin, Z. Chen, P. Bi, Y. Yang, J. Zhang, Z. Huang, Z. Wei, C. An, H. Yao, X. Hao, T. Zhang, Y. Cui, L. Hong, C. Liu, Y. Zu, C. He, J. Hou, 17% efficiency all-small-molecule organic solar cells enabled by nanoscale phase separation with a hierarchical branched structure, Energy Environ. Sci. 14 (2021) 5903–5910.

[27] R. Qin, D. Wang, G. Zhou, Z.-P. Yu, S. Li, Y. Li, Z.-X. Liu, H. Zhu, M. Shi, X. Lu, C.-Z. Li, H. Chen, Tuning terminal aromatics of electron acceptors to achieve high-efficiency organic solar cells, J. Mater. Chem. 7 (2019) 27632–27639.

[28] Z. Zhou, W. Liu, G. Zhou, M. Zhang, D. Qian, J. Zhang, S. Chen, S. Xu, C. Yang, F. Gao, H. Zhu, F. Liu, X. Zhu, Subtle molecular tailoring induces significant morphology optimization enabling over 16% efficiency organic solar cells with efficient charge generation, Adv. Mater. 32 (2020), 1906324.

[29] Q. Fan, H. Fu, Q. Wu, Z. Wu, F. Lin, Z. Zhu, J. Min, H.Y. Woo, A.K.y. Jen, Multi-Selenophene-containing narrow bandgap polymer acceptors for all-polymer solar cells with over 15 % efficiency and high reproducibility, Angew. Chem. Int. Ed. 60 (2021) 15935–15943.

[30] C. Labanti, M.J. Sung, J. Luke, S. Kwon, R. Kumar, J. Hong, J. Kim, A.A. Bakulin, S.-K. Kwon, Y.-H. Kim, J.-S. Kim, Selenium-substituted non-fullerene acceptors: a route to superior operational stability for organic bulk heterojunction solar cells, ACS Nano 15 (2021) 7700–7712.

[31] C. Li, J. Song, Y. Cai, G. Han, W. Zheng, Y. Yi, H.S. Ryu, H.Y. Woo, Y. Sun, Heteroatom substitution-induced asymmetric A-D-A type non-fullerene acceptor for efficient organic solar cells, J. Energy Chem. 40 (2020) 144–150.

[32] K.-K. Liu, X. Xu, J.-L. Wang, C. Zhang, G.-Y. Ge, F.-D. Zhuang, H.-J. Zhang, C. Yang, Q. Peng, J. Pei, Achieving high-performance non-halogenated nonfullerene acceptor-based organic solar cells with 13.7% efficiency via a synergistic strategy of an indacenodithieno[3,2-b]selenophene core unit and non-halogenated thiophene-based terminal group, J. Mater. Chem. 7 (2019) 24389–24399.

[33] S. Shi, J. Yuan, G. Ding, M. Ford, K. Lu, G. Shi, J. Sun, X. Ling, Y. Li, W. Ma, Improved all-polymer solar cell performance by using matched polymer acceptor, Adv. Funct. Mater. 26 (2016) 5669–5678.

[34] S.-S. Wan, C. Chang, J.-L. Wang, G.-Z. Yuan, Q. Wu, M. Zhang, Y. Li, Effects of the number of bromine substitution on photovoltaic efficiency and energy loss of benzo[1,2-b:4,5-b′]diselenophene-based narrow-bandgap multibrominated nonfullerene acceptors, Solar RRL 3 (2019), 1800250.

[35] S.-S. Wan, X. Xu, Z. Jiang, J. Yuan, A. Mahmood, G.-Z. Yuan, K.-K. Liu, W. Ma, Q. Peng, J.-L. Wang, A bromine and chlorine concurrently functionalized end group for benzo[1,2-b:4,5-b ']diselenophene-based non-fluorinated acceptors: a new hybrid strategy to balance the crystallinity and miscibility of blend films for enabling highly efficient polymer solar cells, J. Mater. Chem. 8 (2020) 4856–4867.

[36] F. Wu, W. Gao, H. Yu, L. Zhu, L. Li, C. Yang, Efficient small-molecule non-fullerene electron transporting materials for high-performance inverted perovskite solar cells, J. Mater. Chem. 6 (2018) 4443–4448.

[37] H. Yu, Z. Qi, J. Zhang, Z. Wang, R. Sun, Y. Chang, H. Sun, W. Zhou, J. Min, H. Ade, H. Yan, Tailoring non-fullerene acceptors using selenium-incorporated heterocycles for organic solar cells with over 16% efficiency, J. Mater. Chem. 8 (2020) 23756–23765.

[38] Z. Zhang, Y. Li, G. Cai, Y. Zhang, X. Lu, Y. Lin, Selenium heterocyclic electron acceptor with small urbach energy for as-cast high-performance organic solar cells, J. Am. Chem. Soc. 142 (2020) 18741–18745.

[39] L. Meng, H.-H. Gao, S. Wu, Y. Sun, X. Wan, Y. Yang, J. Wang, Z. Guo, H. Chen, C. Li, Y. Chen, Structural optimization of acceptor molecules guided by a semi-empirical model for organic solar cells with efficiency over 15, Sci. China Mater. 64 (2021) 2388–2396.

[40] Y. Shen, A.R. Hosseini, M.H. Wong, G.G. Malliaras, How to make ohmic contacts to organic semiconductors, ChemPhysChem 5 (2004) 16–25.

[41] C.M. Proctor, M. Kuik, N. Thuc-Quyen, Charge carrier recombination in organic solar cells, Prog. Polym. Sci. 38 (2013) 1941–1960.

[42] D. Credgington, F.C. Jamieson, B. Walker, N. Thuc-Quyen, J.R. Durrant, Quantification of geminate and non-geminate recombination losses within a solution-processed small-molecule bulk heterojunction solar cell, Adv. Mater. 24 (2012) 2135–2141.

[43] L.J.A. Koster, V.D. Mihailetchi, H. Xie, P.W.M. Blom, Origin of the light intensity dependence of the short-circuit current of polymer/fullerene solar cells, Appl. Phys. Lett. 87 (2005), 203502.

[44] A.K.K. Kyaw, D.H. Wang, C. Luo, Y. Cao, T.-Q. Nguyen, G.C. Bazan, A.J. Heeger, Effects of solvent additives on morphology, charge generation, transport, and recombination in solution-processed small-molecule solar cells, Adv. Energy Mater. 4 (2014), 1301469.

[45] C.M. Proctor, C. Kim, D. Neher, N. Thuc-Quyen, Nongeminate recombination and charge transport limitations in diketopyrrolopyrrole-based solution-processed small molecule solar cells, Adv. Funct. Mater. 23 (2013) 3584–3594.

[46] P. Schilinsky, C. Waldauf, C.J. Brabec, Recombination and loss analysis in polythiophene based bulk heterojunction photodetectors, Appl. Phys. Lett. 81 (2002) 3885–3887.

[47] R.D. Jansen-van Vuuren, A. Armin, A.K. Pandey, P.L. Burn, P. Meredith, Organic photodiodes: the future of full color detection and image sensing, Adv. Mater. 28 (2016) 4766–4802.

[48] M.S. Choi, S. Chae, H.J. Kim, J.J. Kim, Control of crystallinity in PbPc:C-60 blend film and application for inverted near-infrared organic photodetector, ACS Appl. Mater. Interfaces 10 (2018) 25614–25620.

[49] N. Gasparini, A. Gregori, M. Salvador, M. Biele, A. Wadsworth, S. Tedde, D. Baran, I. McCulloch, C.J. Brabec, Visible and near-infrared imaging with nonfullerene-based photodetectors, Adv. Mater. Technol. 3 (2018), 1800104.

[50] X. Gong, M.H. Tong, Y.J. Xia, W.Z. Cai, J.S. Moon, Y. Cao, G. Yu, C.L. Shieh, B. Nilsson, A.J. Heeger, High-detectivity polymer photodetectors with spectral response from 300 nm to 1450 nm, Science 325 (2009) 1665–1667.

[51] J.F. Han, D.Z. Yang, D.G. Ma, W.Q. Qiao, Z.Y. Wang, Low-bandgap polymers for high-performance photodiodes with maximal EQE near 1200 nm and broad spectral response from 300 to 1700 nm, Adv. Opt. Mater. 6 (2018), 1800038.

[52] J. Lee, S.-J. Ko, H. Lee, J. Huang, Z. Zhu, M. Seifrid, J. Vollbrecht, V.V. Brus, A. Karki, H. Wang, K. Cho, T.-Q. Nguyen, G.C. Bazan, Side-chain engineering of nonfullerene acceptors for near-infrared organic photodetectors and photovoltaics, ACS Energy Lett. 4 (2019) 1401–1409.
[53] Y. Yao, Y.Y. Liang, V. Shrotriya, S.Q. Xiao, L.P. Yu, Y. Yang, Plastic near-infrared photodetectors utilizing low band gap polymer, Adv. Mater. 19 (2007) 3979–3983.
[54] M. Young, J. Suddard-Bangsund, T.J. Patrick, N. Pajares, C.J. Traverse, M.C. Barr, S.Y. Lunt, R.R. Lunt, Organic heptamethine salts for photovoltaics and detectors with near-infrared photoresponse up to 1600 nm, Adv. Opt. Mater. 4 (2016) 1028–1033.
[55] Z.M. Zhong, L.J. Bu, P. Zhu, T. Xiao, B.B. Fan, L. Ying, G.H. Lu, G. Yu, F. Huang, Y. Cao, Dark current reduction strategy via a layer-by-layer solution process for a high-performance all-polymer photodetector, ACS Appl. Mater. Interfaces 11 (2019) 8350–8356.
[56] Z.M. Zhong, K. Li, J.X. Zhang, L. Ying, R.H. Xie, G. Yu, F. Huang, Y. Cao, High-performance all-polymer photodetectors via a thick photoactive layer strategy, ACS Appl. Mater. Interfaces 11 (2019) 14208–14214.